Origin of Defects and Positron Annihilation in Hybrid and All-Inorganic Perovskites

Artem Musiienko, Jakub Čížek, Hassan Elhadidy, Petr Praus, Kate Higgins, Bogdan Dryzhakov, Andrii Kanak, Franck Sureau, Jindřich Pipek, Eduard Belas, et al.

Origin of Defects and Positron Annihilation in Hybrid and All-Inorganic Perovskites

Artem Musiienko[1*], Jakub Čížek[2], Hassan Elhadidy[3], Petr Praus[3], Kate Higgins[4], Bogdan Dryzhakov[4], Andriy Kanak[5], Franck Sureau[6], Jindřich Pipek[3], Eduard Belas[3], Eric Lukosi[7], Bin Hu[4], Mahshid Ahmadi[4*]

[1]*Helmholtz-Zentrum Berlin für Materialien und Energie GmbH, 12489 Berlin, Kekuléstrasse 5, Germany*

[2] *Charles University, Faculty of Mathematics and Physics, Department of Low-temperature Physics, Prague 8, CZ-18000, Czech Republic*

[3]*Charles University, Faculty of Mathematics and Physics, Institute of Physics, Ke Karlovu 5, CZ-121 16, Prague 2, Czech Republic*

[4]*Joint Institute for Advanced Materials, Department of Materials Science and Engineering, University of Tennessee, Knoxville, TN 37996, USA*

[5]*Yuriy Fedkovych Chernivtsi National University, 2 Str. Kotsiubinskogo, Chernivtsi, Ukraine*

[6]*Laboratoire Jean Perrin, Sorbonne University, Case Courrier 114, 4 Place Jussieu, 75005 Paris, France*

[7]*Joint Institute for Advanced Materials, Department of Nuclear Engineering, University of Tennessee, Knoxville, TN 37996, USA*

Corresponding authors emails:

[*]artem.musiienko@helmholtz-berlin.de,

[*]mahmadi3@utk.edu

Abstract: The emerging metal halide perovskites (MHP) have shown advanced charge transport properties suitable for application in solar cells, photodetectors and various other optoelectronic devices. The stability and uncontrolled defect structure are the main drawbacks limiting the efficient development of MHP devices. This study fills the gap in the understanding of recombination pathways in hybrid and all-inorganic perovskites. We resolved surface and bulk charge transport by combining current waveform time of flight (CW-ToF) and time-resolved photoluminescence (TRPL) spectroscopies. Further, by applying Raman and Infrared spectroscopies, we reveal the nature of the defects associated naturally with solvent trapping. We demonstrated that solvent-associated defects have a substitutional effect on the charge transport efficiency and stability of the MHP devices. Finally, we show the fundamental interaction of positron particles with perovskite vacancy defects and lattice. The positron annihilation is explained by using the *ab-initio* simulation of supercell. The results of this study suggest potential pathways for further improvement of hybrid and all-inorganic MHPs.

Keywords: Perovskites, defects, charge transport, radiation sensors, positron annihilation.

Lead halide perovskites with the formula $APbX_3$, where A^+ is either cesium (Cs), methylammonium (MA) or formamidinium and X^- is either chlorine (Cl), bromine (Br) or iodine (I^-), have emerged as promising candidates for ionizing radiation detectors because of their high attenuation coefficient, tunable band-gap[1-3], large mobility-lifetime ($\mu\tau$) product[1, 2, 4] and low charge trap density and defect tolerance[2, 5-8]. In particular, the all-inorganic cesium lead bromide ($CsPbBr_3$) perovskite is advantageous over its organic-inorganic perovskite counterparts due to its long-term chemical and structural stability[8-12]. Recently, more researchers have shown that $CsPbBr_3$ can achieve high-resolution detection of ionizing radiation[13, 14] in addition to their excellent potential for application in tandem solar cells and LED technology[15, 16].

Until recently, the growth of large-size, high-quality $CsPbBr_3$ single crystals required high-temperature growth from melts using the Bridgman melt-growth method[13]. As this melt-growth method requires temperatures over 500 ˚C and multiple purification steps to purify the raw materials, this increases the cost of device fabrication to a level not lower than other radiation detection materials, such as CdZnTe[14]. Therefore, the need for an inexpensive solution-based growth method is imperative. Over the past few years, the solution-based growth of $CsPbBr_3$ has been demonstrated[11, 17] through the utilization of methods, such as the antisolvent vapor assisted[12, 18] and the inverse temperature crystallization methods[9, 19, 20]. Despite progress in solution-based growth of lead halide perovskite single crystals, the crystallinity, dimensions, and charge transport properties of melt grown single crystals are superior.

It is well established that defects in semiconductor lattice have a critical effect on the performance of semiconductor devices. The crucial charge transport properties such as carrier mobility, lifetime, and recombination rate are greatly affected by the concentration of the defects[8]. The effect of defects on charge transport properties of solution grown perovskites was broadly discussed in our recent studies[21, 22]. Here, we explore the electrical structure, charge transport, and defects chemistry in solution and melt grown lead halide perovskite single crystals to reveal pathways to efficient and cheap perovskite semiconductor devices.

Positron annihilation spectroscopy (PAS) is commonly used to study defects and their chemical nature in various semiconductors[23-26]. In conventional PAS, the material is bombarded with positrons. These positrons are then annihilated by the material's electrons, producing two 511 keV gamma rays. The positron annihilation rate is determined by the local electron density at the positron annihilation site[27]. Because the electron density of a defect site is comparatively less than the electron density of the bulk material, the positron is trapped in a defect site for a longer time. Another positron annihilation technique, Coincidence Doppler Broadening (CDB) spectroscopy of the annihilation gamma rays, provides information about the electron

momentum distribution in a material. Together, these techniques are incredibly powerful in characterizing the chemical nature of defects in a material.

Very few studies have used PAS to characterize the nature of defects in lead halide perovskites. Dhar *et al.* demonstrated the utilization of PAS in combination with Doppler broadening techniques to reveal the presence of MA defects in the $MAPbI_3$ crystal lattice[28]. Particularly, single crystalline $MAPbI_3$ contains few defects than its polycrystalline counterpart but has an equal probability of developing both cationic and anionic (halide) vacancies, whereas the polycrystalline sample contains mainly cationic vacancies in its lattice. PAS has yet to be used to characterize the defects of other lead halide perovskites including $CsPbBr_3$ and $MAPbBr_3$ single crystals.

The free charge carrier losses at the surface, bulk, and interfaces are the main recombination pathways in semiconductor optoelectronic devices. Here, we first compare free charge recombination dynamics at the surface and in the bulk of hybrid and all-inorganic lead bromide perovskites using photoluminescence (PL) and time of flight current waveform (ToF-CW) spectroscopies. As can be seen in (Figure 1) there is a small deviation in the PL spectra of Bridgman grown $CsPbBr_3$, solution grown $CsPbBr_3$, and $MAPbBr_3$ single crystals with bandgap energies of 2.34 eV, 2.33 eV, and 2.31 eV, respectively. In addition, the excitation of the samples at 445 nm wavelength induces a bright luminescence emitted from the surface of these crystals, as shown in Figure 1 due to the presence of surface defects. Time-resolved photoluminescence (TRPL) measurements reveal nanosecond decay of PL signal in all studied samples (Figure 2). A faster and slower decay constants of around 40 ns and 140 ns is observed in $MAPbBr_3$ single crystal (Figure 2a). While the melt (Bridgman) and solution grown $CsPbBr_3$ crystals show decay constants of around 7 ns and 100 ns, and 2 ns and 37 ns, respectively.

To further explore charge carrier lifetime in these crystals, time of flight -current waveform (ToF-CW) spectroscopy was performed. The holes (generated by a short 1 μs laser pulse with a wavelength of 450 nm) drift in the bulk of lead halide perovskite crystals and induce ToF current waveform. Thus, the ToF CW reveals bulk recombination dynamics and lifetime of charge carriers. Recently we showed that charge trapping in the bulk defects is responsible for ToF CW decay[21]. Here, the ToF spectroscopy reveals microsecond dynamics of free holes drifting from anode to the cathode (Figure 2b) under an applied bias of 60 V. To estimate the lifetime of free holes in the bulk, we fit the ToF transients by an exponential fit. Interestingly, $CsPbBr_3$ crystal grown from melt shows holes lifetime of around τ_{CS} =210 μs and $MAPbBr_3$ crystal shows holes lifetime of around τ_{CS} =95 μs. While the $CsPbBr_3$ crystal grown from solution did not show a reliable ToF signal. Other studies also highlighted the critical effect of surface recombination on

TRPL measurements[29]. These results clearly explain the notable difference in charge decay dynamics shown by TRPL and ToF by different recombination rates at the surface and in the bulk of the lead halide perovskites.

Next, we utilized Raman spectroscopy and Fourier-transform infrared spectroscopy (FT-IR) to study the origin of defects and explain the superior transport properties of melt grown $CsPbBr_3$. Firstly, the Raman spectra, specifically at low wavenumbers, of solution grown $MAPbBr_3$, solution grown $CsPbBr_3$, and melt grown $CsPbBr_3$ single crystals provide information regarding the vibrational modes of the metal-halide sublattice[30], as shown in (Figure 3a). Regarding, The observed Raman peaks below 200 cm^{-1} in $MAPbBr_3$ are consistent with the literature and are attributed to lattice vibrations[31]. Next, we note that the Raman spectra for both the solution-grown and melt grown $CsPbBr_3$ are similar. As shown in (Figure 3a) with arrows, the broad peaks around 73 cm^{-1} and 127 cm^{-1}, have previously been reported as the vibration mode of $[PbBr_6]^{4-}$ octahedron and the motion of the Cs^+ cations[32, 33]. Noticeably, we also see a shoulder peak at around 70 cm^{-1} for both the solution grown and melt-grown $CsPbBr_3$. The peak has also been observed in the Raman spectrum of melt grown Cs_4PbBr_6 single crystals[34], indicating a possible second phase on the surface of these single crystals.

We proceeded further by obtaining the Raman spectra at higher wavenumbers to explore molecular modes, as shown in (Figure 3b). Overall, the Raman spectra for the solution grown $MAPbBr_3$ single crystal is consistent with the literature as the higher-frequency peaks being related to the different kinds of the MA^+ cation motions, such as the 918 cm^{-1} and 968 cm^{-1} being attributed to the $CH_3NH_3^+$ rocking and C-N stretching, respectively[35, 36]. Next, we compare the Raman spectra for the solution grown $CsPbBr_3$ and melt grown $CsPbBr_3$ single crystals. Noticeably, the spectra for the solution grown $CsPbBr_3$ single crystal contains well-defined peaks, whereas these peaks are absent for the melt grown $CsPbBr_3$ single crystal. We attribute these peaks shown in the solution-grown $CsPbBr_3$ single crystal to peaks commonly seen in the spectrum for dimethyl sulfoxide (DMSO)[37], which is the solvent used for our growth process. In this Raman spectra peaks at 678 cm^{-1} and 713 cm^{-1} are attributed to C-S symmetric and antisymmetric stretches, and the peak at 1000 cm^{-1} is assigned to the S=O stretch. Further, individual peak assignments for both the solution grown $MAPbBr_3$ and solution grown $CsPbBr_3$ single crystals are shown in Table 1.

We utilize FT-IR characterization as shown in (Figure 3c) to further confirm solvent trapping within solution grown single crystals. Our measured FT-IR spectrum of the solution-grown $MAPbBr_3$ single crystal is consistent with literature[38, 39]. Prominent peaks are at 969 cm^{-1}, 1477 cm^{-1}, 1584 cm^{-1}, and 3165 cm^{-1}, which can be attributed to the C-N stretch, symmetric

NH_3^+ bend, asymmetric NH_3^+ bend, and symmetric NH_3^+ stretch, respectively. As seen with the Raman characterization, there are noticeably defined peaks, such as 951 cm^{-1}, 1028 cm^{-1}, and 1482 cm^{-1}, for the solution grown $CsPbBr_3$ single crystal that are not observed for the melt grown $CsPbBr_3$ single crystal. We attribute these peaks to the solvent trapped within the single crystal as most of these peaks correspond to peaks observed in the FT-IR spectrum for dimethyl sulfoxide (DMSO) as described in Table 1. In Figure 3c, we compare the FT-IR spectrum of DMSO to the solution grown $CsPbBr_3$ to further illustrate this point. Trapped solvent can form point defects and defect complexes responsible for the shorter carrier lifetime in solution grown single crystals. In addition, the trapped solvent can deteriorate the stability of the perovskite devices. For both the solution grown and melt grown $CsPbBr_3$ single crystals, we attribute a few visibly low intensity peaks at 1600 cm^{-1} and 3500 cm^{-1} to the environment, specifically water vibrational modes, as these measurements were performed in ambient conditions[40].

Table 1. Individual peak assignments for both the solution grown $MAPbBr_3$ and solution grown $CsPbBr_3$ single crystals at high wavenumbers.

Raman Shift	Solution-grown $MAPbBr_3$ Peak Assignment	Solution-grown $CsPbBr_3$ Peak Assignment	FT-IR Peak (cm^{-1})	Solution-grown $CsPbBr_3$ Peak Assignment
678	-	C-S Symmetric Stretch	1028	S=O
713	-	C-S Asymmetric Stretch	1308	$-CH_3$ Symmetric
887	-	-	1399	$-CH_3$ Asymmetric
918	$CH_3NH_3^+$ (rocking)	-	1432	$-CH_3$ Asymmetric
968	C-N stretching	-	2909	$-CH_3$ Vibrations
1000		S=O Stretch	2982	$-CH_3$ Vibrations
1252	CH_3-NH_3^+ rocking	-		
1345	-	C-H Symmetric Deformation		
1411	-	CH_3 Degenerate Deformation		
1426	-	-		
1477	Asymmetric NH_3^+ bending	-		
1587	NH_3^+ twisting	-		

Next, to study the possible origin of point defects affecting free charges in single crystals, we study positron interaction we study positron interaction with bulk defects in melt grown $CsPbBr_3$ and $MAPbBr_3$ by positron annihilation positron annihilation spectroscopy (PAS) in picosecond (ps) timescale (

Figure 3 d-e). In this method, Positron implanted into the sample is thermalized within a few ps, i.e. its energy is quickly decreased down to thermal energy, kT. Thermalized positron is delocalized in the lattice as a modulated Bloch-as a modulated Bloch-like wave. Open volume defects, e.g. vacancies, represent potential wells for positron. Hence, if a for positron. Hence, if a sample contains open volume defects, the delocalized positron is trapped in these defects and its

in these defects and its density becomes confined in the defect which is convenient for the study of defects in materials. of defects in materials. Both $CsPbBr_3$ and $MAPbBr_3$ perovskites exhibit a single component decay according to the decay according to the positron lifetime spectra shown in

Figure 3 d-e. Positron decay show an insignificant change of positron lifetime in samples grown by different methods ($CsPbBr_3$: melt and $MAPbBr_3$: solution). By fitting the positron lifetime spectra, $CsPbBr_3$ and $MAPbBr_3$ single crystals show positron lifetimes of 349.6 ps and 343.2 ps, respectively.

To explain the positron lifetime decay, we performed *ab-initio* calculations of lifetimes of positrons annihilated in various states based on local density approximation (LDA)[41]. More details of this calculation can be found in Supplementary materials. The calculated electron density found in bulk and at different vacancies are shown in (Figure 4 a-d). The calculated electron and positron density in the (001) plane for a perfect lattice and various defects in $CsPbBr_3$ are shown in Figure 4 e-h. Results of *ab-initio* calculations of positron lifetimes for various positron states in $CsPbBr_3$ and $MAPbBr_3$ (according to Eq. S1 and Figure 4) are summarized in Table 2. A cation vacancy (Cs-vacancy in $CsPbBr_3$ and MA-vacancy in $MAPbBr_3$) represents a deep positron trap in both compounds. Pb and Br vacancies are capable of positron trapping as well, but positron binding energy to these vacancies is smaller than to the Cs or MA cation vacancies. Positron binding energy to the vacancy is the difference between the ground state energy of delocalized (free) positron and energy of positron trapped in the vacancy. The modeled vacancies show larger *ab-initio* lifetimes than we observed in the positron annihilation experiment.

To explain positron decay, we further considered the annihilation of the positron in a free state, which is a lattice without defects. The calculated bulk positron lifetimes according to Eq. S1 and (Figure 4 a and e) for a perfect lattice of $CsPbBr_3$ and $MAPbBr_3$ are around 355.1 and 333.4 ps, respectively. The bulk (lattice) positron lifetimes found from the experiment are close to the positron lifetimes measured in both crystals. The difference in positron lifetime (several tens of ps) in $CsPbBr_3$ and $MAPbBr_3$ crystals can be explained by the interaction of positrons with different lattices. Due to different cations (MA and Cs), the lattice has slightly different cation radii and lattice constant. As a result, positron trapping and positron lifetimes are slightly different for inorganic and hybrid lead halide perovskites, which was confirmed by *ab-initio* calculations.

Table 2 Results of *ab-initio* calculations of positron lifetimes for a perfect lattice (bulk) and various types of vacancies. Calculated binding energy (E_B) of positron to vacancies is shown in the table as well.

$CsPbBr_3$	τ (ps)	E_B (eV)	$MAPbBr_3$	τ (ps)	E_B (eV)
Experimental PAS lifetime	349.6	-	Experimental PAS lifetime	343.2	-
bulk	355.1	-	bulk	333.4	-
Cs-vacancy	364.8	0.329	MA-vacancy	357.9	0.055
Pb-vacancy	371.9	0.023	Pb-vacancy	347.0	0.010
Br-vacancy	394.8	0.066	Br-vacancy	342.9	0.011

Doppler broadening PAS method can bring additional information about the local chemical environment of defects. The momentum distribution of annihilating electron-positron can be calculated from the first principles and be directly compared with the experimental results. The present approach describes well the high momentum part ($p > 10 \times 10^{-3}$ m_0c) of the momentum distribution of annihilating pair with dominating contribution of core electrons which are localized in atomic shells retaining their atomic character. For the sake of comparison with the experiment, the calculated momentum distributions are presented as ratio curves with respect to Aluminium (Al), i.e. the calculated momentum distributions were divided by the momentum distribution calculated for a perfect Al crystal with an FCC structure and lattice parameter of a = 4.0495 Å.

Coincidence Doppler broadening (CDB) ratio curves (related to pure Al reference) are plotted in (Figure 4 i). Calculated ratio curves for a perfect (defect-free) $CsPbBr_3$ and $MAPbBr_3$ lattice are shown in (Figure 4 j). The *ab-initio* calculations of CDB curves are not accurate enough to allow for quantitative comparison with the experimental results. Nevertheless, there is clearly a good qualitative agreement between CDB curves calculated for perfect (defect-free) $CsPbBr_3$ and $MAPbBr_3$ lattice and experiment. A local maximum at $p \approx 8 \times 10^{-3}$ m_0c followed by a minimum at $p \approx 13 \times 10^{-3}$ m_0c and a broad peak located at higher momenta observed in the experimental curves are well reproduced in calculated curves. $MAPbBr_3$ exhibits a lower peak at $p \approx 8 \times 10^{-3}$ m_0c and position of the local minimum and the following broad peak are shifted to slightly at higher momenta compared to $CsPbBr_3$. This is reproduced in the calculated curves as well. Hence, it can be concluded that CDB data are in agreement with results in Figure 3c that positrons in both samples ($CsPbBr_3$ and $MAPbBr_3$) are annihilated predominantly in the free state, i.e. not trapped at defects. Positron annihilates at the bulk of perovskites interacting with

lattice but not with defects. Due to proven positron annihilation in the lattice of lead bromide perovskite crystals, we can estimate the maximum vacancy concentration to be around 10^{15} cm^{-3} by considering a lower sensitivity limit of positron annihilation spectroscopy for negatively charged vacancies due to the dominance of delocalized bulk state and low positron trapping rate[42].

In summary, comparing the charge decay by TRPL and ToF, we can conclude that these two methods show different decay dynamics. Free carriers drifting in the ToF experiment are mainly affected by defects in the bulk of perovskites. Meanwhile, surface quality has a substantial effect on PL decay. TRPL does not reflect the lifetime of charge carriers in the bulk of perovskites. The dominant charge losses occur at the surface defects with a recombination lifetime of several to hundreds of nanoseconds. The bulk charge transport shows a much longer lifetime of hundreds of microseconds. Among studied hybrid and inorganic lead bromide perovskites, the $CsPbBr_3$ crystal grown from melt show a longer lifetime of charge carrier from bulk, 210 μs. We attribute the difference in charge transport properties between melt and solution grown crystals to solvent trapping within solution grown single crystals. DMSO peaks were detected by Raman and FT-IR spectroscopies in solution grown single crystals. By analyzing the PAS results, we conclude that positrons annihilate in the free state (i.e. not trapped at defects) in both all-inorganic and hybrid perovskite semiconductors grown by different methods. From a comparison of measured experimental positron lifetimes and Doppler broadening with *ab-initio* calculations, $CsPbBr_3$ grown from solution and melt and solution grown $MAPbBr_3$ show a similar mechanism of positron annihilation in the lattice. Thus, both inorganic and hybrid perovskites do not contain defects capable of positron trapping i.e. the concentration of vacancies is lower than $\approx 10^{15}$ cm^{-3}.

This study clarifies the impact of growth conditions on the performance of hybrid and all-inorganic radiation sensors. The comparison of the fundamental properties of single crystals grown from the melt and solution gives valuable information needed for further development of perovskite materials. The demonstrated defect nature and recombination channels reveal further pathways that can lead to more efficient, stable, and cheap perovskite devices.

Methods

Single Crystal Solution Growth

The $MAPbBr_3$ and $CsPbBr_3$ single crystals were grown using the inverse temperature crystallization method[43]. MABr (99.99% from Greatcell Solar Materials), CsBr (99.999% from SigmaAldrich), and $PbBr_2$ (99.999% from SigmaAldrich) were used without further purification.

For $MAPbBr_3$, a molar ratio of 1.2 to 1 of MABr to $PbBr_2$ were dissolved in N,N-Dimethylformamide (99.8% anhydrous from SigmaAldrich) for a 1M solution. For $CsPbBr_3$, a molar ratio of 1 to 2 of CsBr to $PbBr_2$ were dissolved in Dimethyl Sulfoxide (99.9% anhydrous from SigmaAldrich) for a 1M solution[44]. Both solutions were filtered using a 0.2 μm PTFE membrane syringe filter. Crystals precipitated during gradual heating at a rate of 5 ˚C/day from room temperature to ~70 ˚C for $MAPbBr_3$ and ~120 ˚C for $CsPbBr_3$.

Single Crystal Bridgman technique

$CsPbBr_3$ crystals were grown by the Bridgman technique. CsBr (6N) and $PbBr_2$ (5N) (manufactured by Alfa Aesar) in equimolar amounts were loaded in a quartz ampoule and evacuated to 10^{-5} mbar. The ampoule then was sealed and placed in a three-zone vertical furnace. Synthesis of perovskite occurred by the fusion of starting materials. The ampoule with components was slowly heated to a temperature of 645C which exceeding the melting points of both reagents. At this temperature, an isothermal holding was carried out for several hours to achieve melt homogenization and complete the reaction between CsBr and $PbBr_2$. Thereafter, the furnace was cooled down to room temperature for 20 hours. The next step was growing a single crystal of $CsPbBr_3$. The ampoule with the synthesized material was slowly heated up to 585 ° C and lowered with a rate of 3 mm/h into the "cold" zone of the furnace until the ingot crystallization was complete. After this, lowering was stopped and the grown crystal was slowly cooled down to room temperature for 30 hours.

Photoluminescent Spectroscopy

Photoluminescence (PL) and time-resolved photoluminescence measurements (TRPL) were performed using a Horiba Fluorolog3 spectrometer. A 405 nm CW laser was used for excitation during PL measurements. A 343 nm pulsed laser (280 fs, 200kHz) was used for TRPL measurements at the peak emission intensity.

Luminescence measurements

Confocal microspectrofluorimeter adapted for time–resolved fluorescence measurements by using a phase–modulation principle with homodyne data acquisition was employed to obtain fluorescence spectra of Perovskite samples and to determine the fluorescence lifetimes. Laser diode module (Omicron LDM 442.50.A350, Germany) with sinusoidal intensity modulation (50 mW peak output, attenuated to one to tens of μW at the sample) was used for the excitation at 445 nm wavelength. Confocal epifluorescence upright microscope (Zeiss UMSP–80, Germany) with a 10× objective was used to collect the fluorescence emission signal from excited volume of the sample. It is focused on the entrance slit of the Jobin–Yvon HR640 spectrograph equipped

with a 100 line/mm grating. The spectral detection window (375 nm wide) covered both the excitation wavelength (elastic scattering provided us a lifetime reference) and the perovskite emission spectrum. The fluorescence lifetime was calculated from the frequency-dependent phase shift and the intensity demodulation for modulation frequencies covering evenly 5 – 165 MHz interval. Calculated phase differences and modulation ratios are used as an input table for GLOBAL fitting program (Laboratory for Fluorescence Dynamics, Irvine, USA) to calculate single fluorescence lifetime components and their percentage spectral representation.

Raman Spectroscopy and FT-IR Measurements

Raman spectroscopy was carried out on a HORIBA XploRA PLUS Raman system with a 785nm laser at 1mW through a confocal microscope with a 100x objective lens. Multiple scans were averaged for each measurement between 600-2500cm^{-1}. FT-IR spectroscopy on uncrushed single crystals and dimethyl sulfoxide (DMSO) was performed on the Thermo-Scientific Nicolet iS50 FT-IR.

Positron annihilation spectroscopy

A ^{22}Na radioisotope with an activity of ≈1 MBq sealed between two Mylar foils with a thickness of 2 μm.was used as a positron source. A digital spectrometer with a time resolution of 145 ps (FWHM of the resolution function) was used for positron lifetime measurements. Fitting of positron lifetime spectra was performed using the PLRF code[45]. The source contribution to the LT spectra consisted of (i) a component with lifetime of ≈368 ps and relative intensity of ≈10% representing a contribution of positrons annihilated in the source spot and inside the Mylar foil, and (ii) a weak long lived component with lifetime of ≈1.5 ns and intensity of ≈1% originating from pick-off annihilation of ortho-positronium formed in the covering Mylar foil. The CDB studies were carried out using a digital spectrometer equipped with two high-purity Ge detectors. The CDB spectrometer was characterized by an energy resolution of 0.9 keV at the annihilation line and a peak-to-background ratio higher than 10^5. The results of the CDB measurements are presented in this paper as ratio curves related to a well-annealed pure Al (99.9999%) reference sample.

Positron annihilation ab-initio calculations

Positron annihilation related parameters (positron lifetimes and momentum distribution of annihilating electron-positron pairs) were calculated using the density functional theory (DFT). Ab-initio calculations of positron parameters were performed within the so-called standard scheme[46]. In this approximation, positron density is assumed to be everywhere vanishingly small

and not affecting the bulk electron structure. Modeling of point defects was performed using 320 atom-based supercells consisting of 4 × 4 × 4 perovskite units. Vacancies were created simply by removing corresponding atoms. Details of calculations of positron lifetimes are described in the Supplementary materials.

Acknowledgment:

K.H., B.D., E.L., B.H. and M.A. acknowledge financial support from US Department of Homeland Security (grant # 2016-DN-077-ARI01).

Commentaire [MA1]: All authors provide acknowlgment

References:

1. Wei, H.; DeSantis, D.; Wei, W.; Deng, Y.; Guo, D.; Savenije, T. J.; Cao, L.; Huang, J., Dopant compensation in alloyed CH3NH3PbBr3−xClx perovskite single crystals for gamma-ray spectroscopy. *Nature Materials* **2017,** *16* (8), 826-833.
2. Wei, H.; Huang, J., Halide lead perovskites for ionizing radiation detection. *Nat Commun* **2019,** *10* (1), 1066.
3. Sutton, R. J.; Eperon, G. E.; Miranda, L.; Parrott, E. S.; Kamino, B. A.; Patel, J. B.; Hörantner, M. T.; Johnston, M. B.; Haghighirad, A. A.; Moore, D. T.; Snaith, H. J., Bandgap-Tunable Cesium Lead Halide Perovskites with High Thermal Stability for Efficient Solar Cells. *Advanced Energy Materials* **2016,** *6* (8).
4. Yakunin, S.; Dirin, D. N.; Shynkarenko, Y.; Morad, V.; Cherniukh, I.; Nazarenko, O.; Kreil, D.; Nauser, T.; Kovalenko, M. V., Detection of gamma photons using solution-grown single crystals of hybrid lead halide perovskites. *Nature Photonics* **2016,** *10* (9), 585-589.
5. Dong Shi, V. A., Riccardo Comin, Mingjian Yuan, Erkki Alarousu,Andrei Buin,Yin Chen,Sjoerd Hoogland,Alexander Rothenberger, Khabiboulakh Katsiev, Yaroslav Losovyj, Xin Zhang, Peter A. Dowben, Omar F. Mohammed, Edward H. Sargent, Osman M. Bakr, Low trap-state density and long carrier diffusion in organolead trihalide perovskite single crystals. *Science* **2015,** *347*, 519-522.
6. Wen, X.; Feng, Y.; Huang, S.; Huang, F.; Cheng, Y.-B.; Green, M.; Ho-Baillie, A., Defect trapping states and charge carrier recombination in organic–inorganic halide perovskites. *J. Mater. Chem. C* **2016,** *4* (4), 793-800.
7. Zheng, X.; Chen, B.; Dai, J.; Fang, Y.; Bai, Y.; Lin, Y.; Wei, H.; Zeng, Xiao C.; Huang, J., Defect passivation in hybrid perovskite solar cells using quaternary ammonium halide anions and cations. *Nature Energy* **2017,** *2* (7), 17102.
8. Kang, J.; Wang, L. W., High Defect Tolerance in Lead Halide Perovskite CsPbBr3. *J Phys Chem Lett* **2017,** *8* (2), 489-493.
9. Dirin, D. N.; Cherniukh, I.; Yakunin, S.; Shynkarenko, Y.; Kovalenko, M. V., Solution-Grown CsPbBr3 Perovskite Single Crystals for Photon Detection. *Chem Mater* **2016,** *28* (23), 8470-8474.
10. Stoumpos, C. C.; Malliakas, C. D.; Peters, J. A.; Liu, Z.; Sebastian, M.; Im, J.; Chasapis, T. C.; Wibowo, A. C.; Chung, D. Y.; Freeman, A. J.; Wessels, B. W.; Kanatzidis, M. G., Crystal Growth of the Perovskite Semiconductor CsPbBr3: A New Material for High-Energy Radiation Detection. *Crystal Growth & Design* **2013,** *13* (7), 2722-2727.
11. Ding, J.; Du, S.; Zuo, Z.; Zhao, Y.; Cui, H.; Zhan, X., High Detectivity and Rapid Response in Perovskite CsPbBr3 Single-Crystal Photodetector. *The Journal of Physical Chemistry C* **2017,** *121* (9), 4917-4923.

12. Rakita, Y.; Kedem, N.; Gupta, S.; Sadhanala, A.; Kalchenko, V.; Böhm, M. L.; Kulbak, M.; Friend, R. H.; Cahen, D.; Hodes, G., Low-Temperature Solution-Grown CsPbBr3 Single Crystals and Their Characterization. *Crystal Growth & Design* **2016,** *16* (10), 5717-5725.
13. He, Y.; Matei, L.; Jung, H. J.; McCall, K. M.; Chen, M.; Stoumpos, C. C.; Liu, Z.; Peters, J. A.; Chung, D. Y.; Wessels, B. W.; Wasielewski, M. R.; Dravid, V. P.; Burger, A.; Kanatzidis, M. G., High spectral resolution of gamma-rays at room temperature by perovskite CsPbBr3 single crystals. *Nat Commun* **2018,** *9* (1), 1609.
14. Feng, Y.; Pan, L.; Wei, H.; Liu, Y.; Ni, Z.; Zhao, J.; Rudd, P. N.; Cao, L. R.; Huang, J., Low defects density CsPbBr3 single crystals grown by an additive assisted method for gamma-ray detection. *J. Mater. Chem. C* **2020**.
15. Ahn, N.; Kwak, K.; Jang, M. S.; Yoon, H.; Lee, B. Y.; Lee, J.-K.; Pikhitsa, P. V.; Byun, J.; Choi, M., Trapped charge-driven degradation of perovskite solar cells. *Nature Communications* **2016,** *7* (1), 13422.
16. Duan, J.; Zhao, Y.; Wang, Y.; Yang, X.; Tang, Q., Hole-Boosted Cu(Cr,M)O2 Nanocrystals for All-Inorganic CsPbBr3 Perovskite Solar Cells. *Angew. Chem. Int. Ed.* **2019,** *58* (45), 16147-16151.
17. Saidaminov, M. I.; Haque, M. A.; Almutlaq, J.; Sarmah, S.; Miao, X.-H.; Begum, R.; Zhumekenov, A. A.; Dursun, I.; Cho, N.; Murali, B.; Mohammed, O. F.; Wu, T.; Bakr, O. M., Inorganic Lead Halide Perovskite Single Crystals: Phase-Selective Low-Temperature Growth, Carrier Transport Properties, and Self-Powered Photodetection. *Advanced Optical Materials* **2017,** *5* (2).
18. Zhang, H.; Liu, X.; Dong, J.; Yu, H.; Zhou, C.; Zhang, B.; Xu, Y.; Jie, W., Centimeter-Sized Inorganic Lead Halide Perovskite CsPbBr3 Crystals Grown by an Improved Solution Method. *Crystal Growth & Design* **2017,** *17* (12), 6426-6431.
19. Wang, F.; Zhang, H.; Sun, Q.; Hafsia, A. B.; Chen, Z.; Zhang, B.; Xu, Y.; Jie, W., Low-Temperature Solution Growth and Characterization of Halogen (Cl, I)-Doped CsPbBr3 Crystals. *Crystal Growth & Design* **2020,** *20* (3), 1638-1645.
20. Zhang, H.; Wang, F.; Lu, Y.; Sun, Q.; Xu, Y.; Zhang, B.-B.; Jie, W.; Kanatzidis, M. G., High-sensitivity X-ray detectors based on solution-grown caesium lead bromide single crystals. *J. Mater. Chem. C* **2020,** *8* (4), 1248-1256.
21. Musiienko, A.; Pipek, J.; Praus, P.; Brynza, M.; Belas, E.; Dryzhakov, B.; Du, M.-H.; Ahmadi, M.; Grill, R., Deciphering the effect of traps on electronic charge transport properties of methylammonium lead tribromide perovskite. *Science Advances* **2020,** *6* (37), eabb6393.
22. Musiienko, A.; Moravec, P.; Grill, R.; Praus, P.; Vasylchenko, I.; Pekarek, J.; Tisdale, J.; Ridzonova, K.; Belas, E.; Landová, L.; Hu, B.; Lukosi, E.; Ahmadi, M., Deep levels, charge transport and mixed conductivity in organometallic halide perovskites. *Energy & Environmental Science* **2019,** *12* (4), 1413-1425.
23. Guin, S. N.; Banerjee, S.; Sanyal, D.; Pati, S. K.; Biswas, K., Origin of the Order–Disorder Transition and the Associated Anomalous Change of Thermopower in AgBiS2 Nanocrystals: A Combined Experimental and Theoretical Study. *Inorganic Chemistry* **2016,** *55* (12), 6323-6331.
24. Guin, S. N.; Pan, J.; Bhowmik, A.; Sanyal, D.; Waghmare, U. V.; Biswas, K., Temperature Dependent Reversible p–n–p Type Conduction Switching with Colossal Change in Thermopower of Semiconducting AgCuS. *Journal of the American Chemical Society* **2014,** *136* (36), 12712-12720.
25. Grebennikov, D.; Ovchar, O.; Belous, A.; Mascher, P., Application of positron annihilation and Raman spectroscopies to the study of perovskite type materials. *Journal of Applied Physics* **2010,** *108* (11), 114109.
26. Pansara, P. R.; Meshiya, U. M.; Makadiya, A. R.; Raval, P. Y.; Modi, K. B.; Nambissan, P. M. G., Defect structure transformation during substitution in quadruple perovskite

CaCu3-xTi4-xFe2xO12 studied by positron annihilation spectroscopy. *Ceramics International* **2019,** *45* (15), 18599-18603.
27. Sundar, C. S., Positron annihilation spectroscopy in materials science. *Bulletin of Materials Science* **1994,** *17* (7), 1215-1232.
28. Dhar, J.; Sil, S.; Dey, A.; Sanyal, D.; Ray, P. P., Investigation of Ion-Mediated Charge Transport in Methylammonium Lead Iodide Perovskite. *The Journal of Physical Chemistry C* **2017,** *121* (10), 5515-5522.
29. Weiss, T. P.; Bissig, B.; Feurer, T.; Carron, R.; Buecheler, S.; Tiwari, A. N., Bulk and surface recombination properties in thin film semiconductors with different surface treatments from time-resolved photoluminescence measurements. *Scientific Reports* **2019,** *9* (1), 5385.
30. Cha, J. H.; Noh, K.; Yin, W.; Lee, Y.; Park, Y.; Ahn, T. K.; Mayoral, A.; Kim, J.; Jung, D. Y.; Terasaki, O., Formation and Encapsulation of All-Inorganic Lead Halide Perovskites at Room Temperature in Metal-Organic Frameworks. *J Phys Chem Lett* **2019,** *10* (9), 2270-2277.
31. Wang, K.-H.; Li, L.-C.; Shellaiah, M.; Wen Sun, K., Structural and Photophysical Properties of Methylammonium Lead Tribromide (MAPbBr3) Single Crystals. *Scientific Reports* **2017,** *7* (1), 13643.
32. Calistru, D. M.; Mihut, L.; Lefrant, S.; Baltog, I., Identification of the symmetry of phonon modes in CsPbCl3 in phase IV by Raman and resonance-Raman scattering. *Journal of Applied Physics* **1997,** *82* (11), 5391-5395.
33. Shibata, K.; Yan, J.; Hazama, Y.; Chen, S.; Akiyama, H., Exciton Localization and Enhancement of the Exciton–LO Phonon Interaction in a CsPbBr3 Single Crystal. *The Journal of Physical Chemistry C* **2020,** *124* (33), 18257-18263.
34. Cha, J. H.; Han, J. H.; Yin, W.; Park, C.; Park, Y.; Ahn, T. K.; Cho, J. H.; Jung, D. Y., Photoresponse of CsPbBr3 and Cs4PbBr6 Perovskite Single Crystals. *J Phys Chem Lett* **2017,** *8* (3), 565-570.
35. Xie, L. Q.; Zhang, T. Y.; Chen, L.; Guo, N.; Wang, Y.; Liu, G. K.; Wang, J. R.; Zhou, J. Z.; Yan, J. W.; Zhao, Y. X.; Mao, B. W.; Tian, Z. Q., Organic-inorganic interactions of single crystalline organolead halide perovskites studied by Raman spectroscopy. *Phys Chem Chem Phys* **2016,** *18* (27), 18112-8.
36. Wang, K. H.; Li, L. C.; Shellaiah, M.; Wen Sun, K., Structural and Photophysical Properties of Methylammonium Lead Tribromide (MAPbBr3) Single Crystals. *Sci Rep* **2017,** *7* (1), 13643.
37. Batista, A. N. L.; Batista Jr, J. M.; Bolzani, V. S.; Furlan, M.; Blanch, E. W., Selective DMSO-induced conformational changes in proteins from Raman optical activity. *Physical Chemistry Chemical Physics* **2013,** *15* (46), 20147-20152.
38. Mahapatra, A.; Parikh, N.; Kumari, H.; Pandey, M. K.; Kumar, M.; Prochowicz, D.; Kalam, A.; Tavakoli, M. M.; Yadav, P., Reducing ion migration in methylammonium lead tribromide single crystal via lead sulfate passivation. *Journal of Applied Physics* **2020,** *127* (18).
39. Xie, L. Q.; Chen, L.; Nan, Z. A.; Lin, H. X.; Wang, T.; Zhan, D. P.; Yan, J. W.; Mao, B. W.; Tian, Z. Q., Understanding the Cubic Phase Stabilization and Crystallization Kinetics in Mixed Cations and Halides Perovskite Single Crystals. *J Am Chem Soc* **2017,** *139* (9), 3320-3323.
40. Zhang, M.; Zheng, Z.; Fu, Q.; Chen, Z.; He, J.; Zhang, S.; Chen, C.; Luo, W., Synthesis and single crystal growth of perovskite semiconductor CsPbBr 3. *Journal of Crystal Growth* **2018,** *484*, 37-42.
41. Boroński, E.; Nieminen, R. M., Electron-positron density-functional theory. *Physical Review B* **1986,** *34* (6), 3820-3831.

42. Gebauer, J.; Rudolf, F.; Polity, A.; Krause-Rehberg, R.; Martin, J.; Becker, P., On the sensitivity limit of positron annihilation: detection of vacancies in as-grown silicon. *Applied Physics A* **1999,** *68* (4), 411-416.
43. Saidaminov, M. I.; Abdelhady, A. L.; Murali, B.; Alarousu, E.; Burlakov, V. M.; Peng, W.; Dursun, I.; Wang, L.; He, Y.; Maculan, G.; Goriely, A.; Wu, T.; Mohammed, O. F.; Bakr, O. M., High-quality bulk hybrid perovskite single crystals within minutes by inverse temperature crystallization. *Nature Communications* **2015,** *6*, 7586.
44. Saidaminov, M. I.; Haque, M. A.; Almutlaq, J.; Sarmah, S.; Miao, X.-H.; Begum, R.; Zhumekenov, A. A.; Dursun, I.; Cho, N.; Murali, B.; Mohammed, O. F.; Wu, T.; Bakr, O. M., Inorganic Lead Halide Perovskite Single Crystals: Phase-Selective Low-Temperature Growth, Carrier Transport Properties, and Self-Powered Photodetection. *Advanced Optical Materials* **2017,** *5* (2), 1600704.
45. ČÍŽEk, J., PLRF Code for Decomposition of Positron Lifetime Spectra. *Acta Physica Polonica, A.* **2020,** *137* (2), 177-187.
46. Puska, M. J.; Nieminen, R. M., Theory of positrons in solids and on solid surfaces. *Reviews of Modern Physics* **1994,** *66* (3), 841-897.
47. Alatalo, M.; Barbiellini, B.; Hakala, M.; Kauppinen, H.; Korhonen, T.; Puska, M. J.; Saarinen, K.; Hautojärvi, P.; Nieminen, R. M., Theoretical and experimental study of positron annihilation with core electrons in solids. *Physical Review B* **1996,** *54* (4), 2397-2409.
48. Kuriplach, J.; Morales, A. L.; Dauwe, C.; Segers, D.; Šob, M., Vacancies and vacancy-oxygen complexes in silicon: Positron annihilation with core electrons. *Physical Review B* **1998,** *58* (16), 10475-10483.

TOC GRAPHICS

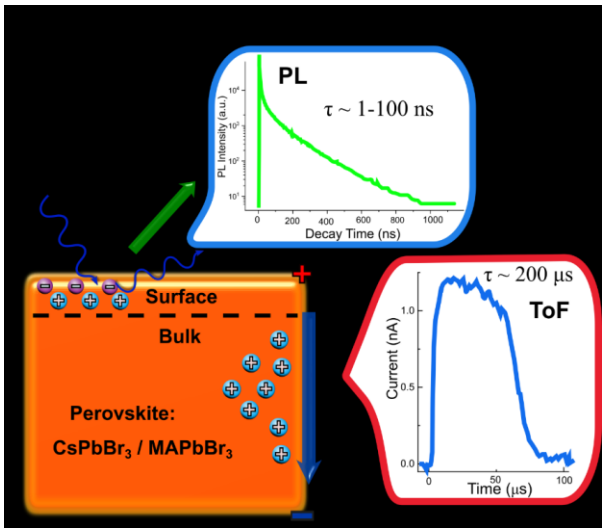

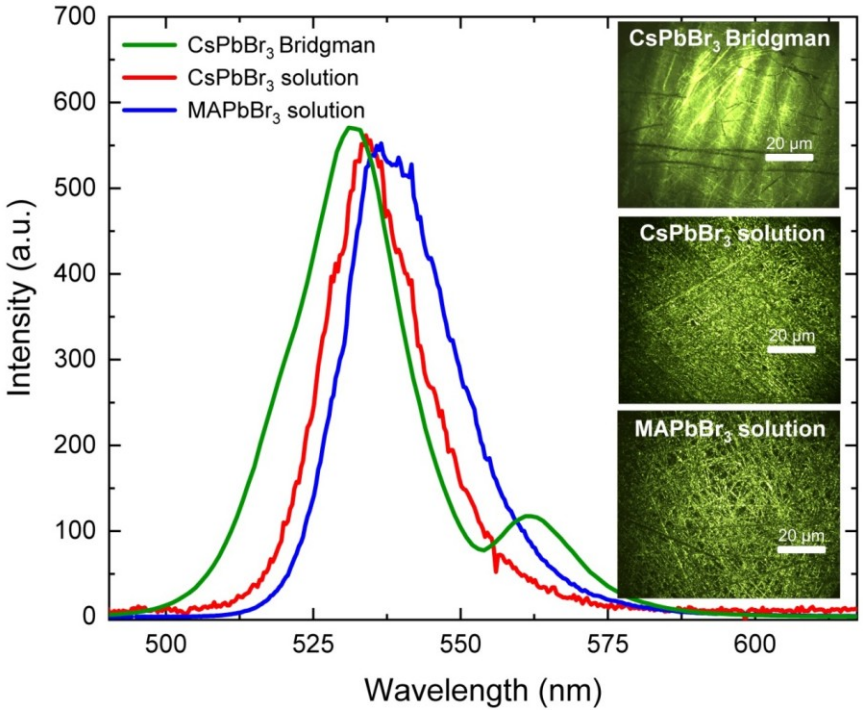

Figure 1 Photoluminescent spectra of $CsPbBr_3$ and $MAPbBr_3$ single crystals grown by melt (Bridgman) and solution methods. (The images on right show the surface emission after the excitation with 445 nm laser. More details can be found in SI Figure S1 and method section.

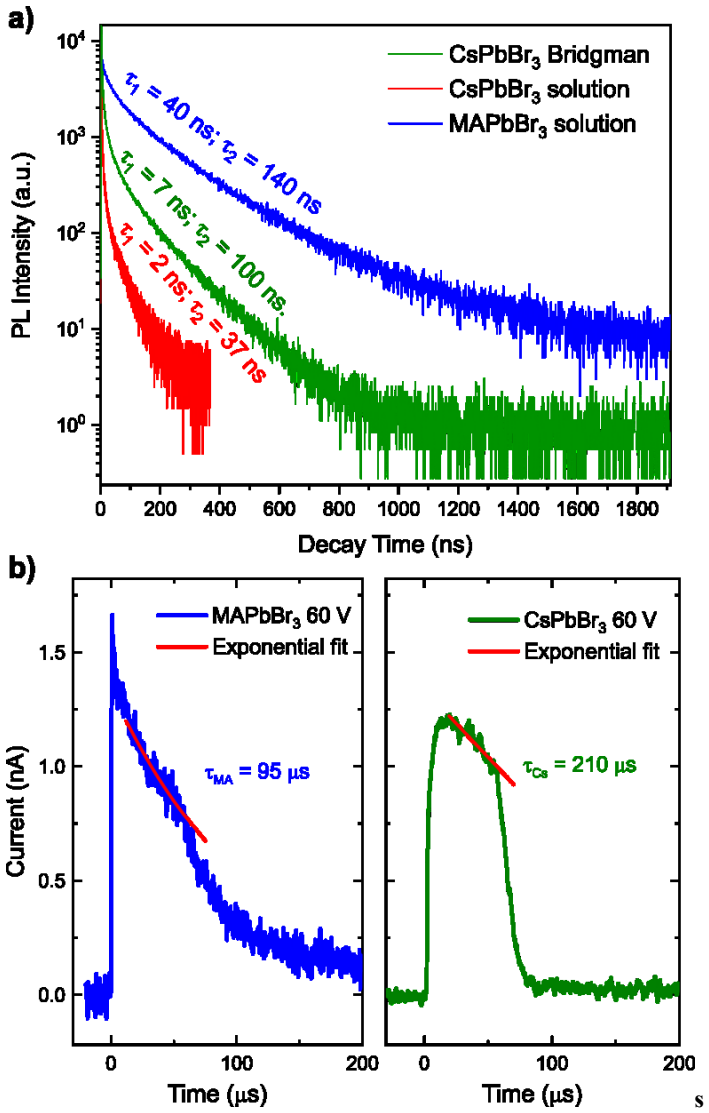

Figure 2 a) Time-resolved photoluminescence (TRPL) decay of $CsPbBr_3$ and $MAPbBr_3$ single crystals grown by melt and solution methods. **b)** Time of Flight current waveform (ToF-CW) decay in melt grown $CsPbBr_3$ and solution grown $MAPbBr_3$ samples.

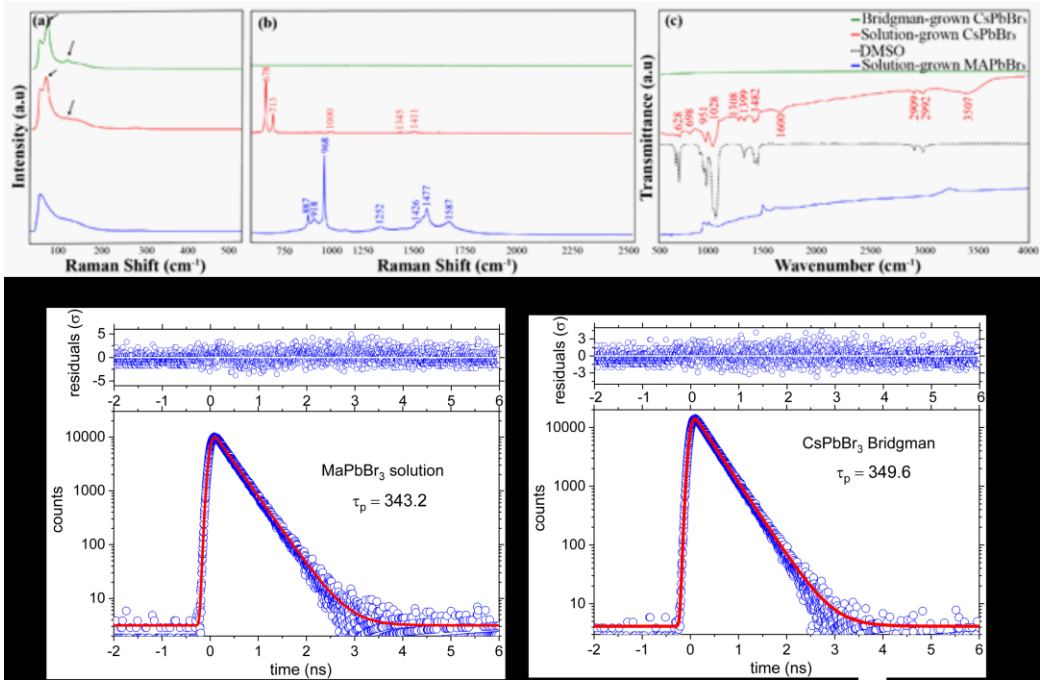

Figure 3 Raman spectra for solution grown $MAPbBr_3$, solution grown $CsPbBr_3$, and melt grown $CsPbBr_3$ single crystals for a) low wavenumbers and b) high wavenumbers. Shown in c) is the FT-IR results for the same crystals. d) and e) Positron lifetime spectra measured in melt grown $CsPbBr_3$ and solution grown $MAPbBr_3$ respectively. The details on the fitting procedure can be found in the method section.

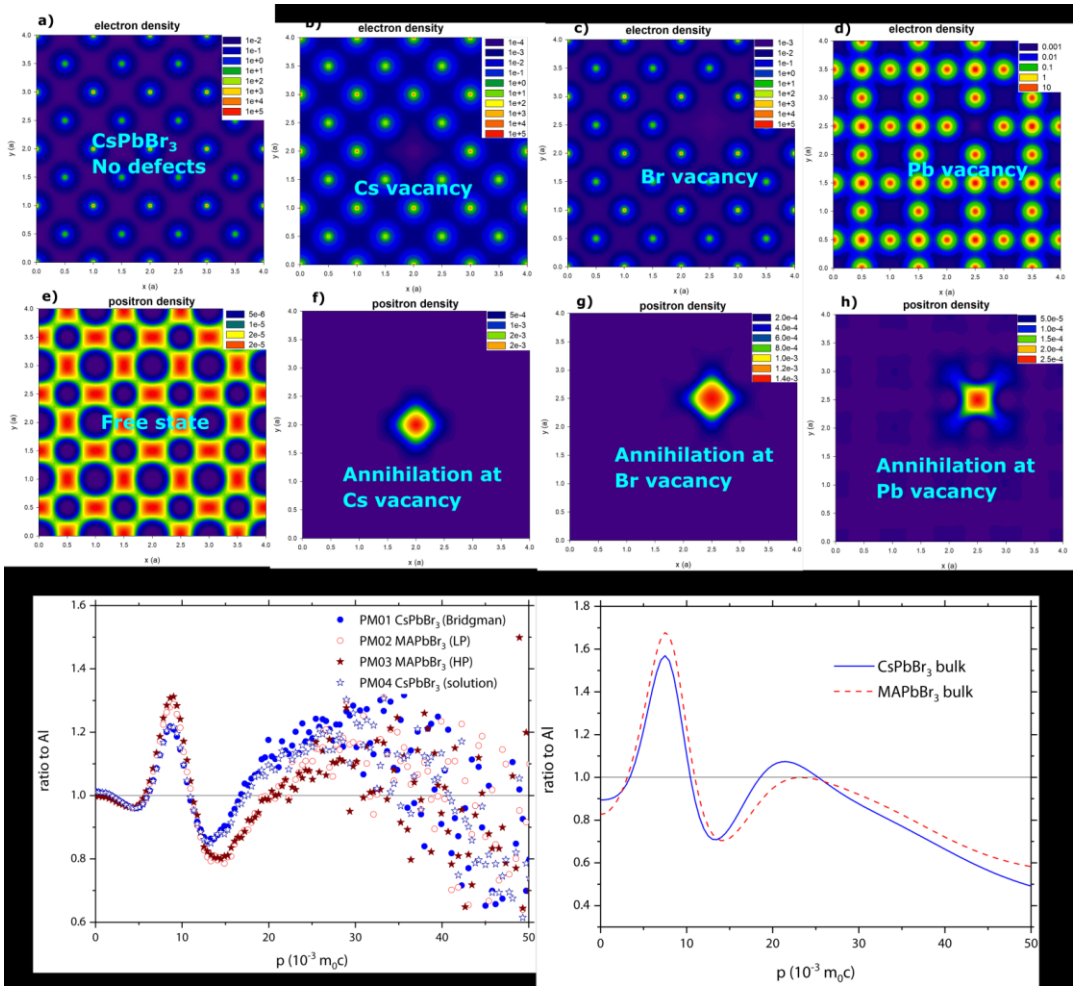

Figure 4 Calculated electron density in the (001) plane for a) $CsPbBr_3$ lattice with no defects, b) Cs vacancy, c) Br vacancy, and d) Pb vacancy, e), f), g), and h) show corresponding positron density obtained from the *Ab-initio* calculations. i) Experimental CDB ratio curves (with respect to Al reference) for $CsPbBr_3$ and $MAPbBr_3$ samples grown by different methods. j) Calculated CDB ratio curves (with respect to pure Al reference) for free positrons in $CsPbBr_3$ and $MAPbBr_3$.

Supplementary Materials

Positron annihilation ab-initio calculations

In the first step the Electron density $n_-(\boldsymbol{r})$ in the material was calculated without presence of positron. Subsequently, the effective potential for positron was constructed as

$$V_+(\boldsymbol{r}) = \phi(\boldsymbol{r}) + V_{corr}\,[n_-, \nabla n_-],$$

where $\phi(r)$ is the Coulomb potential produced by the charge distribution of electrons and nuclei and V_{corr} is the electron-positron correlation potential in the limit of vanishing positron density[46]. In the second step the ground state of positron wave function $\psi_+(\boldsymbol{r})$ was calculated by solving of a single particle Schrödinger equation

$$-\frac{1}{2}\nabla^2\psi_+(\boldsymbol{r}) + \mathrm{V}_+(\boldsymbol{r})\psi_+(\boldsymbol{r}) = E_+\psi_+(\boldsymbol{r}), \qquad \textbf{S(1)}$$

where E_+ is the positron ground state energy.

The positron lifetime is determined from the overlap of the electron density $n_-(\boldsymbol{r})$ and the positron density $n_+(\boldsymbol{r}) = |\psi_+(\boldsymbol{r})|^2$ using the expression

$$\tau = \left\{\pi r_e^2 c \int n_+(\boldsymbol{r}) n_-(\boldsymbol{r}) \gamma[n_-, \nabla n_-] d\boldsymbol{r}\right\}^{-1}, \qquad \textbf{S(2)}$$

where r_e is the classical electron radius and c is the speed of light. An enhancement of electron density at the site of positron due to positron-electron correlation was taken into account through the enhancement factor γ which accounts for an enhancement of the electron density at the site of positron[46]. . The enhancement factor γ and the electron-positron correlation potential V_{corr} were treated within the local density approximation (LDA) using the parametrization by Boronski and Nieminen[41]. Within this approach the enhancement factor γ and the electron-positron correlation potential V_{corr} are determined by the local electron density n_- and its gradient ∇n_- at the positron annihilation site.

The momentum distribution of annihilating electron-positron pairs was calculated using the approach described in[47, 48]. Electrons belonging to a shell of i-th atom described by the principal quantum number n and the angular quantum number l contribute to the momentum distribution by a contribution

$$\rho^{i,nl}(p) = 4\pi^2 r_e^2 c N^{i,nl} \gamma^{i,nl} \left| \int R_+^i R_-^{i,nl} B_l(pr) r^2 dr \right|^2 \qquad \textbf{S(3)}$$

where $N^{i,nl}$ is the number electrons in the shell n,l; B_l is the spherical Bessel function and R_+^i, $R_-^{i,nl}$ denote the radial part of positron and electron wave functions. The symbol $\gamma^{i,nl}$ stands for the state-dependent positron enhancement factor[48]. The total momentum distribution of the annihilating electron-positron pairs was obtained by summing the partial contributions $\rho^{i,nl}(p)$

of electron shells of overall occupied atomic sites and corresponding electron shells. To account for a finite energy resolution of the CDB spectrometer the calculated momentum distributions were convoluted with a Gaussian function with FWHM of 3.5×10^3 m_0c.

Microspectrofluorimeter setup

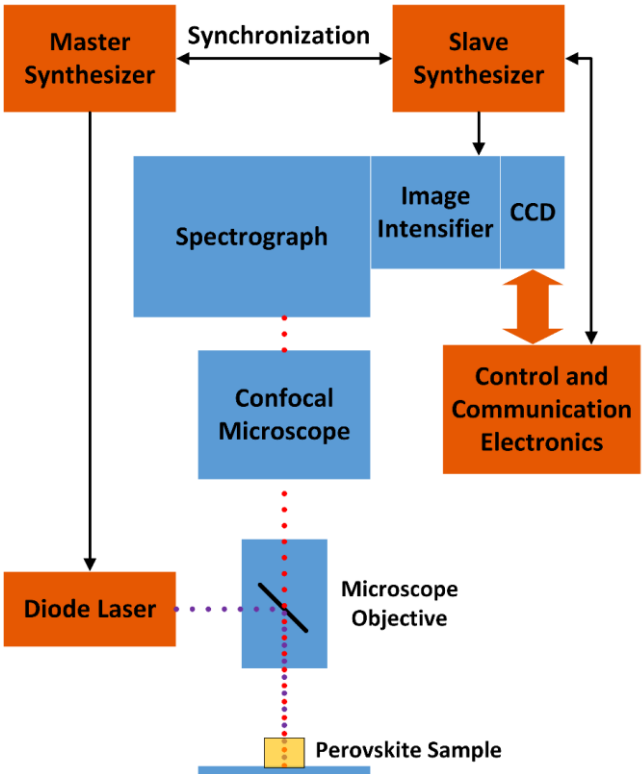

Figure. S1. Block Scheme of the microspectrofluorimeter setup